PHYSICAL REVIEW B VOLUME 4, NUMBER 8 15 OCTOBER 1971

One-Phonon Vibronic Transition ${}^3T_{2g}$- ${}^3A_{2g}$ of Ni^{2+} in MgO†

N. B. Manson*
Department of Physics, University of California, Los Angeles, California 90024

(Received 17 April 1970)

The near infrared emission of MgO : Ni^{2+} at 77 and 5 °K is reported. At helium temperature the spectrum consists of one sharp zero-phonon line between the $\Gamma_{3g}({}^3T_{2g},\ t_{2g}^5e_g^3)$ and $\Gamma_{5g}({}^3A_{2g},\ t_{2g}^6e_g^2)$ states, and an accompanying vibrational sideband. On the assumption that the perturbation giving rise to this sideband comes from an interaction of the impurity ion with its nearest neighbors, the intensity of the band can be described in terms of a weighted sum of localized Green's functions. A calculation of these functions is made based on a lattice-dynamical shell model. By taking a semiempirical admixture of the various calculated Green's functions, a good comparison with the one-phonon sideband is obtained. The agreement is shown to remain fair when using admixtures determined by considering a model where the Ni^{2+} ion experiences a varying electrostatic potential because of the motion of point-charge nearest neighbors.

I. INTRODUCTION

Several studies have been made on the vibronic spectra of rare-earth ions[1–5] and color centers[6,7] in alkali halide lattices for which the lattice dynamics had been previously determined with the help of neutron and x-ray diffraction data. A knowledge of the lattice dynamics permits a computation of the vibrational sideband distribution which can be compared with the spectrum to test the theoretical model. Until recently,[8] no such treatment has been presented for the case of $3d^n$-$3d^n$ transitions, but these iron-group ions substitute for Mg^{2+} in the MgO lattice, giving, in several cases (Ni^{2+}, V^{2+}, Cr^{3+}, Mn^{4+}),[9–13] interesting detailed vibrational sidebands. Furthermore,[14] Peckham has used a shell-model treatment of the lattice dynamics of MgO to give fair agreement with neutron data,[14,15] so that this system is an ideal one for the above type of study.

In the case of the rare-earth ions, an electrostatic coupling model is used which considers the perturbation giving rise to the sideband as coming from the varying electric field of the phonons at the impurity site.[1–5] However, for the iron-group ions, the $3d^n$ electrons lie outermost on the ion and overlap the surrounding ions (e.g., see Ref. 16), so that the perturbation giving rise to the phonon-assisted transitions should depend largely on the motion of the nearest neighbors.

Both this paper (I) and the following paper (II)[17] present calculations of vibronic transitions of MgO : Ni^{2+} made within this framework of nearest-neighbor coupling interaction. In this paper, attention is restricted to one-phonon sidebands and the $\Gamma_{3g}({}^3T_{2g},\ t_{2g}^5e_g^3) \rightarrow \Gamma_{5g}({}^3A_{2g},\ t_{2g}^6e_g^2)$ transition of the Ni^{2+} ion. The vibronic intensity is expressed in terms of a weighted sum of odd-parity localized Green's functions. These functions are determined from a numerical calculation of the lattice-dynamical shell model with allowance made for possible mass and nearest-neighbor force-constant changes. On substituting Ni^{2+} for Mg^{2+} in MgO the mass change is known precisely but some estimation or guess at the force-constant changes have to be made. In Secs. VI and VII, two different sideband constructions are given and compared to the observed vibronic spectrum. In Sec. VI, the admixture of Green's functions is treated semiempirically in an attempt to give a best fit to experimental data. In Sec. VII, a rather crude point-charge model is adopted in an independent calculation of these coupling parameters.

This study complements parallel work done by Sangster and McCombie[8] who have treated the case of the vibronic band ${}^2E_g \rightarrow {}^4A_{2g}$ of V^{2+} in MgO and $\Gamma_{3g}({}^3T_{2g}) \rightarrow \Gamma_{5g}({}^3A_{2g})$ of Ni^{2+} in MgO. Comparisons will be made here with their work.

II. SPECTRUM OF MgO : Ni^{2+}

First, a synopsis of MgO : Ni^{2+} spectrum, both absorption and emission, is made with consideration given to which bands come from single electronic transitions.

Ralph and Townsend[10] have recently published the absorption spectrum of MgO : Ni^{2+} at 77 and 5 °K. This agrees (although in greater detail) with earlier data by Pappalardo, Wood, and Linares[18] and by Low.[19] Three strong absorption bands appear at 8500, 14 500, and 25 000 cm^{-1} corresponding to the spin-allowed transitions from the ${}^3A_{2g}(t_{2g}^6e_g^2)$ ground state to the ${}^3T_{2g}(t_{2g}^5e_g^3)$, ${}^3T_{1g}(t_{2g}^5e_g^3)$, and ${}^3T_{1g}(t_{2g}^4e_g^4)$ states, respectively. A fourth and weaker band at 21 500 cm^{-1} corresponds to the spin-forbidden transition to the ${}^1T_{2g}(t_{2g}^5e_g^3)$ state. For each of the spin-allowed transitions there are several close-lying electronic levels, and each one gives rise to a vibronic band. These overlap and cannot be separated. This makes the absorption data of the spin-allowed bands unsatisfactory for a detailed analysis of the vibronic structure. The spin-forbidden transition is weak and only the predominant features of the structure can be seen, but this will be used in Paper II when discussing this transition.

The fluorescence of a Ni^{2+}-doped MgO crystal has been measured by the author under several different excitation methods including (i) optical lamps—high-pressure mercury arc, zenon arc, quartz-iodine, and tungsten; (ii) a 50-μA, 20-kV electron beam; and (iii) 15-mA, 55-kV white x rays. Several emission bands are seen with identical structure but varying relative intensity, for the different excitation mechanisms. By comparing the spectrum from numerous doped and undoped crystals it was established that two of these bands are associated with the Ni^{2+} center—one in the green at 20 000 cm^{-1} and one in the near infrared at 8 000 cm^{-1}. The third band seen by Ralph and Townsend[10] at 13 000 cm^{-1} was not seen here—masked by very strong emission from other impurity centers.

The infrared emission at 8 000 cm^{-1} has been reported previously by Ralph and Townsend[9] under electron-beam excitation and is reported here under optical excitation. (With the excitation methods available, the fluorescence was an order of magnitude more intense using optical pumping than by electron or x-ray bombardment.) Emission is observed from two electronic levels located at 8 178 and 8 002 cm^{-1} corresponding to the excited states $\Gamma_{4g}({}^3T_{2g},\ t_{2g}^5e_g^3)$ and $\Gamma_{3g}({}^3T_{2g},\ t_{2g}^5e_g^3)$, respectively. From each state there is a zero-phonon line and an associated sideband but, by cooling to helium temperature, where only the lower level is populated, a band associated with a single electronic transition is isolated. This band is predominantly one phonon and is the focus of attention in the present paper.

The second emission band at 21 000 cm^{-1} arises from the ${}^1T_{2g}$ state—an isolated electronic level. The emission, therefore, is associated with a single electronic transition. It is broader than the infrared band and clearly involves more than one-phonon processes. It will be the subject of a detailed study in Paper II where the whole treatment of vibronic transition is extended to consider multiphonon processes.

III. EXPERIMENT DETAILS

The near-infrared emission spectrum of MgO:Ni was recorded for a crystal clamped to a copper finger of a helium Dewar. The crystal had been grown from the melt in an electric-arc furnace[20] with a dopant level of 0.1-wt.% Ni and had dimensions 4×10×10 mm. The fluorescence was stimulated by using a 48-W incandescent tungsten lamp, an $f/1$ condenser lens and filters. The emission at right angles was analyzed by a Bausch and Lomb 0.5-m monochromator with 600 line rulings/mm grating blazed at 1 μ and detected by a PbS cell using phase-sensitive techniques.

At room temperature the fluorescence extends from 8500 to just beyond 7500 cm^{-1} with a broad peak at 7700 cm^{-1}. On cooling, the intensity drops slightly and some structure appears. By liquid nitrogen temperature, the band exhibits one strong sharp peak at 8002 cm^{-1} with several peaks on the low-energy side. On the high-energy side there is a weak sharp peak at 8178 cm^{-1} which disappears if the crystal is further cooled. At helium temperature the emission consists of one strong sharp line then at 8009 cm^{-1}, which is narrower than the instrument can resolve (10 cm^{-1}) accompanied by a sideband which has major peaks at 220, 390, and 555 cm^{-1} and further minor peaks up to a distance of 1000 cm^{-1} from the initial sharp line.

The two sharp fluorescence lines at 8002 and 8178 cm^{-1} at N_2 temperature coincide with the sharp lines in the absorption to the ${}^3T_{2g}(t_{2g}^5e_g^3)$ levels[18] and arise from magnetic dipole pure electron transitions between the two lower Γ_{3g}, Γ_{4g} spin-orbit split components of the ${}^3T_{2g}(t_{2g}^5e_g^3)$ state and the ground state $\Gamma_{5g}({}^3A_{2g},\ t_{2g}^6e_g^2)$.[18] ($\Gamma$ is used to denote irreducible representation of direct products of spin-orbit space.)

The emission at 77 °K agrees with that observed by Ralph and Townsend[20] but at 5 °K differs in the structure within 200 cm^{-1} of the zero-phonon line—presumably due to different crystal preparation or dopant concentration. The peaks, at 90 cm^{-1} and 125 cm^{-1}, which are clearly seen at helium temperatures (Fig. 1) are considered to arise from Ni^{2+} at noncubic sites, probably Ni^{2+} pairs. As the temperature is raised from 5 °K, these lines broaden without any corresponding broadening in the 8009-cm^{-1} line or anywhere in the sideband. The rest of the band is, thus, considered to arise solely from the phonon-assisted $\Gamma_{3g}({}^3\Gamma_{2g}, t_{2g}^5e_g^3) \rightarrow \Gamma_{5g}({}^3A_{2g}, t_{2g}^6, e_g^2)$ transition of the Ni^{2+} ion at cubic sites.

IV. THEORY

It is assumed that when the Ni^{2+} ion replaces the Mg^{2+} ion that there may be a relaxation of the lattice about the impurity-ion site. If the state is degenerate, then this relaxation may lower the symmetry from O_h by the Jahn-Teller effect.[21] In the case of Ni^{2+}, the ground state is an orbital singlet and does not distort other than by an A_{1g} displacement as confirmed by electron spin resonance (ESR) measurements.[22] When in the excited state, an orbital T_{2g}, the system may be distorted but this is assumed to be small enough that the O_h point group may be used to a good approximation.

The equilibrium configuration of the lattice for the Ni^{2+} ion in its ground and in its excited state may differ and result in changes in the lattice vibrations between the two states, i.e., in the

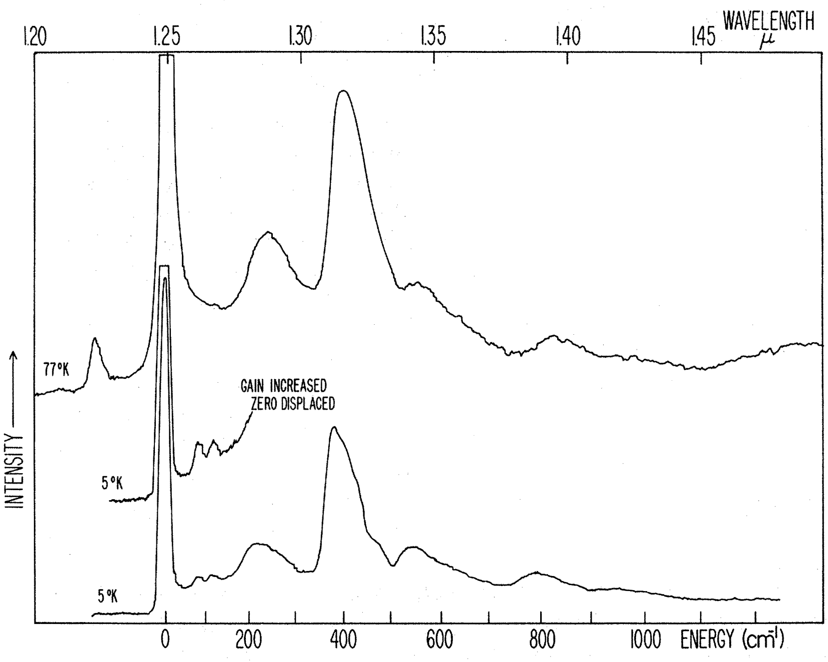

FIG. 1. Emission spectrum of MgO : Ni^{2+} at 5 and 77 °K. The intensity is uncorrected for relative sensitivity but varies by less than 5% across the spectral range.

Green's-function calculation which follows, different force constant changes should be used for the two Ni^{2+} states. Here these changes are assumed to be small so that the same or average force constant changes may be used. If the sideband were observed to be mirror images in absorption and emission, this would be a fair indication that the lattice vibrations were indeed unaltered between the two states. Unfortunately, overlap of neighboring transitions in absorption prevents such a comparison for the transition of present interest. For a second Ni^{2+} transition, $\Gamma_{5g}({}^1T_{2g}t_{2g}^5e_g^3) \to \Gamma_{5g}({}^3A_{2g}t_{2g}^6e_g^2)$, where the distortions are suspected to be larger, the vibronic bands in emission and absorption are close to mirror images of one another[17] and, thus the assumption should be reasonable for both transitions.

The zero-phonon line at 8009 cm^{-1} is a permitted magnetic dipole transition, but the associated sideband is considered to arise from electric dipole radiation induced by odd-parity vibrations about the impurity site. The predominant features of the sideband lie within the range of the vibrations of the MgO lattice and, therefore, the problem of linear electron lattice coupling is of principal interest.

It is assumed that the coupling arises solely from the interaction with nearest neighbors, so the interaction is expanded in a power series of the symmetry displacements

$$V(\vec{r}, X) = V(\vec{r}, 0) + \sum_{\Gamma\gamma n} V_{\Gamma\gamma}^{(n)}(\vec{r})\, X_{\Gamma\gamma}^{(n)} , \qquad (1)$$

where the electronic coupling functions are derivatives of the electron potential evaluated at the equilibrium configuration of the defect lattice:

$$V_{\Gamma\gamma}^{(n)}(\vec{r}) = \left.\frac{\partial V(\vec{r})}{\partial X_{\Gamma\gamma}^{(n)}}\right|_{X=0} . \qquad (2)$$

$\vec{r}$ represents the electron coordinate, X the nucleus coordinate ($X = 0$ for equilibrium configuration of defect lattice), and $X_{\Gamma\gamma}^{(n)}$ the symmetry displacement coordinates of the central ion and six nearest neighbors (called the complex). Γ represents the irreducible representation, and γ the row of that representation according to which the displacement transforms and (n) is used to distinguish between displacements of the same symmetry.

Note that within the complex, the symmetry coordinates $X_{\Gamma\gamma}^{(n)}$ are related to the normal coordinates $q(\vec{k}, j)$ by a linear transformation

$$X_{\Gamma\gamma}^{(n)} = \sum_{\vec{k}j} \mathcal{A}_{\Gamma\gamma}^{(n)}(\vec{k}, j)\, q(\vec{k}, j) . \qquad (3)$$

The total transition probability of going from one electronic level e, symmetry Γ_e, to a second level f, symmetry Γ_f, with the same parity, and generally being degenerate, is given by the sum of the transition probabilities of the component transitions. The pure electric dipole transitions are forbidden by parity, but in second-order perturbation the probability per unit time $W_{e\to f}$ of an electric dipole transition is given by

$$W_{e\to f}=\frac{2\pi}{\hbar}\sum_{\text{initial and final states}}\left|\sum_i\frac{\langle\Psi_f|P+V|\Psi_i\rangle\langle\Psi_i|P+V|\Psi_e\rangle}{E_i-E_e}\right|\delta(E_f-E_e)\,, \tag{4}$$

where P is the interaction with the photon field in the dipole approximation. The Ψ's are total wavefunctions of the system; Ψ_e is the excited state, Ψ_f the ground state, and Ψ_i the intermediate state. E_e, E_f, and E_i are the energies of these states. The summation over initial and final states includes the contribution from the individual transitions between the components of the degenerate levels.

The transition probability for a system initially in the electronic excited state e, and zeroth harmonic-oscillator state (i.e., low-temperature limit) making a transition to the ground electronic state with the creation of one phonon is given by

$$W_{e\to f}=\frac{2\pi}{\hbar}\sum_{\gamma_e\gamma_f}\sum_{\text{final states}}\left|\sum_{a_i\Gamma_i\gamma_i}\left\{\frac{\langle 1\chi_1(\vec{k},j)\Gamma_f\gamma_f|P|0\chi_1(\vec{k},j)\,a_i\Gamma_i\gamma_i\rangle\langle 0\chi_1(\vec{k},j)a_i\Gamma_i\gamma_i|V|0\chi_0(\vec{k},j)\Gamma_e\gamma_e\rangle}{\mathcal{E}_i-\mathcal{E}_e+\hbar\omega(\vec{k},j)}\right.\right.$$
$$\left.\left.+\frac{\langle 1\chi_1(\vec{k},j)\Gamma_f\gamma_f|V|1\chi_0(\vec{k},j)a_i\Gamma_i\gamma_i\rangle\langle 1\chi_0(\vec{k},j)a_i\Gamma_i\gamma_i|P|0\chi_0(\vec{k},j)\Gamma_e\gamma_e\rangle}{\mathcal{E}_i-\mathcal{E}_e-\hbar\omega(\vec{k},j)}\right\}\right|^2\delta(\mathcal{E}_f-\mathcal{E}_e+\hbar\omega(\vec{k},j)+\hbar\nu)\,, \tag{5}$$

where the wavefunctions $|\Psi_k\rangle$ have been written as $|nx_h(\vec{k},j)\Gamma_k\gamma_k\rangle$. n is the number of photons, $\chi_h(\vec{k},j)$ is the harmonic-oscillator wave function for the lattice with all the individual oscillators in their zeroth occupational state except the $(\vec{k},j)$ mode, which is in occupational state h (here, either 1 or 0), and $\Gamma_k\gamma_k$ is the electronic wave function of the state k, symmetry Γ_k, row γ_k (a_k is used in addition where there are more than the one possible state of that symmetry). $\mathcal{E}_k$ is the energy of the electronic level, $\hbar\omega(\vec{k},j)$ the energy of the phonon, and $\hbar\nu$ the energy of the associated photon.

The crystal is cubic and hence the calculation may be continued using only one component of the dipole operator, say y. Then after substitution from Eq. (1), the transition rate for photons with angular frequency between ν and $\nu+\Delta\nu$ observed in solid angle $\Delta\Omega$ is

$$W_{e\to f}=\frac{\Delta\Omega\Delta\nu\nu^3e^2}{2\pi c^3}\sum_{\gamma_e\gamma_f}\sum_{\vec{k}j}\left|\sum_{a_i\Gamma_i\gamma_i}\left\{\frac{\langle\Gamma_f\gamma_f|y|a_i\Gamma_i\gamma_i\rangle\sum_{\Gamma\gamma n}\langle a_i\Gamma_i\gamma_i|V_{\Gamma\gamma}^{(n)}|\Gamma_e\gamma_e\rangle\langle\chi_1(\vec{k},j)|X_{\Gamma\gamma}^{(n)}|\chi_0(\vec{k},j)\rangle}{\mathcal{E}_i-\mathcal{E}_e+\hbar\omega(\vec{k},j)}\right.\right.$$
$$\left.\left.+\frac{\langle a_i\Gamma_i\gamma_i|y|\Gamma_e\gamma_e\rangle\sum_{\Gamma\gamma n}\langle\Gamma_f\gamma_f|V_{\Gamma\gamma}^{(n)}|a_i\Gamma_i\gamma_i\rangle\langle\chi_1(\vec{k},j)|X_{\Gamma\gamma}^{(n)}|\chi_0(\vec{k},j)\rangle}{\mathcal{E}_i-\mathcal{E}_f-\hbar\omega(\vec{k},j)}\right\}\right|^2\delta(\mathcal{E}_f-\mathcal{E}_e+\hbar\omega(\vec{k},j)+\hbar\nu)\,. \tag{6}$$

The dipole matrix elements $\langle\Gamma_f\gamma_f|y|a_i\Gamma_i\gamma_i\rangle$ and $\langle a_i\Gamma_i\gamma_i|y|\Gamma_e\gamma_e\rangle$ will only be nonzero if the states Γ_i have the opposite parity to Γ_f (and Γ_e) which also restricts the coupling function $V_{\Gamma\gamma}^{(n)}$, symmetry Γ, to be of odd parity. The odd-parity excited states $a_i\Gamma_i\gamma_i$ lie well above the $3d^n$ states of concern and, therefore, it may be assumed that $\hbar\omega(\vec{k},j)\ll\mathcal{E}_i-\mathcal{E}_f$ and $\hbar\omega(\vec{k},j)\ll\mathcal{E}_i-\mathcal{E}_e$ for all $\vec{k}$, j. The vibrational and electronic parts in the expression for the transition rate can be further separated to give

$$W_{e\to f}=W(\omega)\Delta\omega=\frac{\Delta\Omega\Delta\nu\nu^3e^2}{2\pi c^3}\sum_{\gamma_e\gamma_f}\sum_{\vec{k}j}\sum_{\Gamma\gamma nn'}F_{y\Gamma\gamma n}^{\gamma_e\to\gamma_f}F_{y\Gamma\gamma n'}^{\gamma_e\to\gamma_f*}\langle\chi_1(\vec{k},j)|X_{\Gamma\gamma}^{(n)}|\chi_0(\vec{k},j)\rangle$$
$$\langle\chi_0(\vec{k},j)|X_{\Gamma\gamma}^{(n')*}|\chi_1(\vec{k},j)\rangle\,\delta(\mathcal{E}_f-\mathcal{E}_e+\hbar\omega(\vec{k},j)+\hbar\nu)\,, \tag{7}$$

where

$$F_{y\Gamma\gamma n}^{\gamma_e\to\gamma_f}=\sum_{a_i\Gamma_i\gamma_i}\left\{\frac{\langle\Gamma_f\gamma_f|y|a_i\Gamma_i\gamma_i\rangle\langle a_i\Gamma_i\gamma_i|V_{\Gamma\gamma}^{(n)}|\Gamma_e\gamma_e\rangle}{\mathcal{E}_i-\mathcal{E}_e}+\frac{\langle\Gamma_f\gamma_f|V_{\Gamma\gamma}^{(n)}|a_i\Gamma_i\gamma_i\rangle\langle a_i\Gamma_i\gamma_i|y|\Gamma_e\gamma_e\rangle}{\mathcal{E}_i-\mathcal{E}_f}\right\}\,. \tag{8}$$

By substituting from Eq. (3) and using harmonic-oscillator creation and annihilation operators, the vibrational part gives

$$\sum_{\vec{k}j}\langle\chi_1(\vec{k},j)|X_{\Gamma\gamma}^{(n)}|\chi_0(\vec{k},j)\rangle\langle\chi_0(\vec{k},j)|X_{\Gamma\gamma}^{(n')*}|\chi_1(\vec{k},j)\rangle$$
$$\times\,\delta(\hbar\omega-\hbar\omega(\vec{k},j))$$
$$=\sum_{\vec{k}j}\mathcal{A}_{\Gamma\gamma}^{(n)}(\vec{k},j)\mathcal{A}_{\Gamma\gamma}^{(n')}(\vec{k},j)^*\frac{1}{2\omega(\vec{k},j)}\,\delta(\omega-\omega(\vec{k},j))$$

$$= \mathrm{Im} \sum_{\vec{k}j} \frac{\mathcal{A}^{(n)}_{\Gamma\gamma}(\vec{k},j)\mathcal{A}^{(n')}_{\Gamma\gamma}(\vec{k},j)^*}{\omega(\vec{k},j)^2 - (\omega + i\epsilon)^2}$$

$$= (1/\pi)\,\mathrm{Im}\,G^{(nn')}_{\Gamma}(\omega)\,, \tag{9}$$

where $\hbar\omega = \mathcal{E}_e - \mathcal{E}_f - \hbar\nu$, the frequency shift from the zero-phonon position. $G^{(nn')}_{\Gamma}(\omega)$ is the standard Green's function of the localized space of the central ion and nearest neighbors, for the pair of symmetry displacements $\Gamma\gamma n$, $\Gamma\gamma n'$ and is independent of the row γ of the irreducible representation; Im stands for "imaginary part."

The one-phonon distribution can finally be written

$$W(\omega) = \frac{\Delta\Omega\nu^3 e^2}{2\pi^2 c^3} \sum_{\Gamma n n'} \left[\sum_{\gamma} \sum_{\gamma_e \gamma_f} F^{\gamma_e \to \gamma_f}_{y\Gamma\gamma n} F^{\gamma_e \to \gamma_f\,*}_{y\Gamma\gamma n'}\right] \mathrm{Im}\,G^{(nn')}_{\Gamma}(\omega)\,, \tag{10}$$

i.e., a superposition of the Green's functions associated with the odd displacements of the complex, weighted by the coupling parameter given in the square bracket.

V. GREEN'S FUNCTIONS

As pointed out by Page and Dick,[6] a Green's-function treatment consistent with the lattice dynamics should include the shell-shell and core-shell as well as core-core functions. This would greatly increase the number of separate functions and hence the number of coupling parameters. However, the functional form of the shell-shell and core-shell Green's functions almost mirror the corresponding core-core functions[23]—essentially because of the strong shell-core force constants—and thus their introduction merely adds to the complexity without necessarily improving agreement. Any better degree of fit could equally well be brought about by variations of the parameters already present. The calculations, therefore, are restricted to the core-core Green's functions even though it will introduce inaccuracies, hopefully small, when considering the defect lattice.

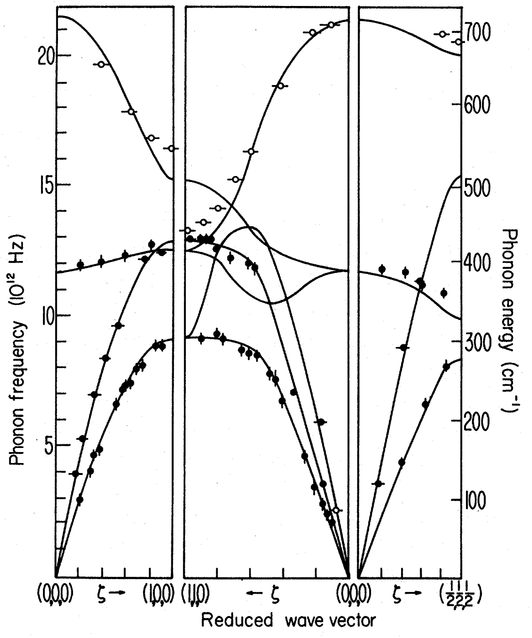

FIG. 2. Phonon dispersion relations along major symmetry directions in MgO. The solid line shows the shell model predictions using the parameters given in Table I. The open and shaded experimental points are those of Peckham (Ref. 14) and Buckland and Saunderson (Ref. 15), respectively. The horizontal and vertical bars through these points denote longitudinal and transverse vibrations, respectively.

TABLE I. Shell model parameters.

Constant		Value	Units	Spring constant in N/m
Mg^{2+}-O^{2-} longitudinal spring constant	A	32.43		204
Mg^{2+}-O^{2-} transverse spring constant	B	−4.26		−26.8
O^{2-}-O^{2-} longitudinal spring constant	A''	−2.49	$e^2/2v$	−15.6
O^{2-}-O^{2-} transverse spring constant	B''	0.37		2.3
O^{2-} shell-core spring constant	k	60.0		377
Mg^{2-} shell-core spring constant		∞		∞
Total charge on each ion	Z	2	e	
O^{2-} shell charge	Y_2	−2.81		
Mg^{2-} mass	m_{Mg}	24.32	a.m.u.	
O^{2-} mass	m_{O_2}	16.0		
Cell constant	R	2.106	Å	

The Green's function computations were made by M. J. Sangster and are reported in some detail in Ref. 8. The shell model employed was that of Peckham.[14] The parameters are shown in Table I and the resultant dispersion curves in directions of high symmetry are indicated in Fig. 2. The agreement with neutron data is always within 13% although in general it is significantly better. The dynamical matrix was solved for 3142 points evenly distributed in $\frac{1}{48}$ of the first Brillouin zone giving 125 000 points in the entire zone. The eigenfrequencies $\omega(\vec{k},j)$ are grouped into 600 equal frequency intervals between 0 and 702 cm^{-1}. Then for one row of each symmetry displacement $\Gamma^{(n)}$, the value of $\mathcal{A}^{(n)}_{\Gamma\gamma}(\vec{k},j)$ is determined by using the relationship

$$\mathcal{A}^{(n)}_{\Gamma\gamma}(\vec{k},j) = X^{(n)}_{\Gamma\gamma}\, q(\vec{k},j)\;. \tag{11}$$

The product $\mathcal{A}^{(n)}_{\Gamma\gamma}(\vec{k},j)\mathcal{A}^{(n')}_{\Gamma\gamma}(\vec{k},j)^*$ gives the contribution to the Green's function $G^{(nn')}_{\Gamma}(\omega)$ from the mode $(\vec{k},j)$ and the total value of the function in a given interval is obtained by summing over all the modes within that interval and dividing by the width of the interval and by twice the frequency. A histogram is formed which is smoothed to give a continuous function

$$\mathrm{Im}\,G_{\Gamma}^{(nn')}(\omega)=\frac{\pi}{\Delta\omega}\sum_{\omega\leq\omega(\vec{k},j)<\omega+\Delta\omega}\frac{\mathcal{A}_{\Gamma\gamma}^{(n)}(\vec{k},j)\mathcal{A}_{\Gamma\gamma}^{(n')}(\vec{k},j)^{*}}{2\omega(\vec{k},j)}. \tag{12}$$

The real part of the Green's function can be obtained by Kramer-Kronig relation

$$\mathrm{Re}\,G_{\Gamma}^{(nn')}(\omega)=\frac{1}{\pi}\,\mathrm{P}\int_{0}^{\omega_{\max}}\frac{\mathrm{Im}\,G_{\Gamma}^{(nn')}(\omega)}{\omega_i^2-\omega^2}\,d\omega_i\,. \tag{13}$$

Re denotes "real part," and P denotes "principal part." $\omega_{\max}$ is the maximum frequency of the lattice.

In an XY_6 complex, there are four even-parity displacements A_{1g}, E_g, T_{1g}, and T_{2g} and hence four associated Green's functions. Also, there are four odd-parity displacements, one T_{2u} and three T_{1u} (Fig. 3) which result in seven associated Green's functions, six related to T_{1u} motions. The effective number of the T_{1u} functions will eventually be greatly reduced (from six to three) by choosing as one of the basis the translational motion of the complex for which there will be no coupling within the present scheme. However, all six must be retained until the imperfect lattice problem is tackled.

When an impurity ion replaces the Mg^{2+} ion there will be in addition to the change of mass at the sites changes in the force constants in its neighborhood. If strongly localized, the changes will be predominantly in the force constant between central ion and the nearest neighbors plus, perhaps, any change of the shell-core spring constant within the central ion. This latter change is discounted since the Ni^{2+} ion does not have appreciable polarizability compared to the oxygen ion. The model adopted then allows for a change in mass, and in longitudinal and transverse force constants ΔA and ΔB between the central ion and the six nearest neighbors, respectively.

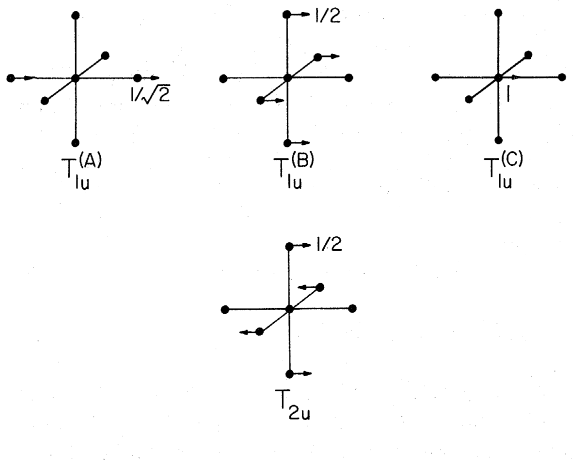

FIG. 3. Odd-parity symmetry displacements of nearest neighbors indicated for one row.

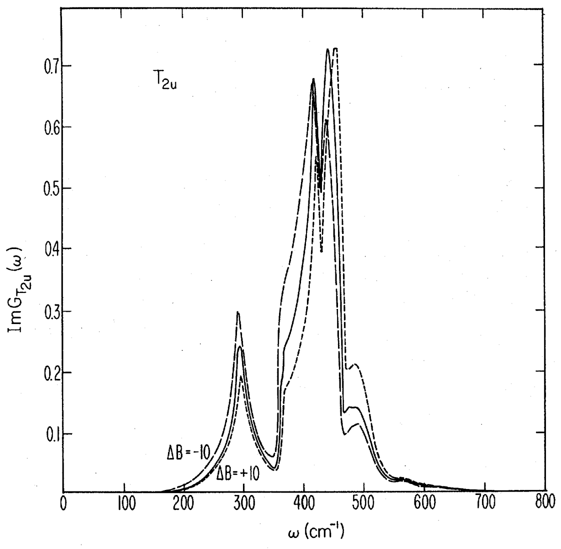

FIG. 4. The imaginary parts of the T_{2u} Green's functions. The solid curve gives the perfect-lattice Green's function and the dashed curves give the functions where changes ΔB (in N/m) have been made in the transverse force constant B. The vertical scale is in units of 10^{-28} sec^2 per atomic mass unit.

The Green's function of the defect lattice is then simply related to the perfect-lattice functions:

$$\underline{G}^{\mathrm{imp}}(\omega)=[\underline{I}+\underline{G}(\omega)\underline{\Delta K}(\omega)]^{-1}\,\underline{G}(\omega)\,, \tag{14}$$

where $\underline{G}(\omega)$ is the matrix of the perfect-lattice Green's functions and $\underline{G}^{\mathrm{imp}}(\omega)$ the equivalent matrix for the imperfect or defect lattice. $\underline{\Delta K}(\omega)$ is the matrix of the local disturbance.

Note that this equation also is not strictly consistent in its treatment of the cores and shells of the dynamical model in that it neglects the very high frequency shell vibrations, which effect all the Green's functions including core-core functions in going from the perfect to defect lattice. [Term $(H_{ss}^{0})^{-1}$ of Born and Wagner[3] is neglected; see Ref. 23.] This omission should not change the Green's functions substantially.

For the T_{2u} motion there is simply the one Green's function in the matrix and the associated element $\Delta K=\Delta B$, the change in the transverse spring constant. The T_{2u} perfect-lattice Green's function is shown by the solid curve in Fig. 4, and the imperfect lattice function for two different changes in the B force constant by the dashed curves.

With the definition of T_{1u} basis functions shown in Fig. 3, the matrix of T_{1u} Green's function is

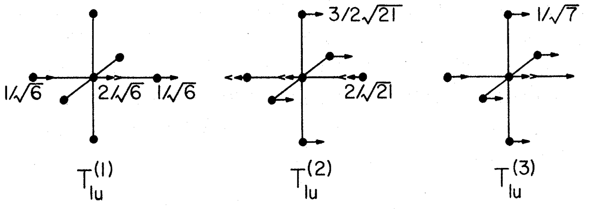

FIG. 5. T_{1u} orthonormal symmetry adapted displacement of central ion and nearest neighbors indicated for one row.

$$\underline{G}(\omega)=\begin{pmatrix} G^{(AA)}(\omega) & G^{(AB)}(\omega) & G^{(AC)}(\omega) \\ G^{(BA)}(\omega) & G^{(BB)}(\omega) & G^{(BC)}(\omega) \\ G^{(CA)}(\omega) & G^{(CB)}(\omega) & G^{(CC)}(\omega) \end{pmatrix}, \tag{15}$$

and the matrix of the local disturbance at the same time is

$$\underline{\Delta K}(\omega)=\begin{pmatrix} \Delta A & 0 & -\sqrt{2}\Delta A \\ 0 & \Delta B & -2\Delta B \\ -\sqrt{2}\Delta A & -2\Delta B & 2\Delta A+4\Delta B-\Delta m \end{pmatrix}. \tag{16}$$

The imperfect-lattice function can then be obtained from Eq. (14). Functions defined in terms of an alternative set of basis vectors as given in Fig. 5 can then be obtained by a linear transformation

$$\underline{S}=\begin{pmatrix} \sqrt{2}/\sqrt{6} & 0 & -2/\sqrt{6} \\ -2\sqrt{2}/\sqrt{21} & 3/\sqrt{21} & -2/\sqrt{21} \\ \sqrt{2}/\sqrt{7} & 2/\sqrt{7} & 1/\sqrt{7} \end{pmatrix}. \tag{17}$$

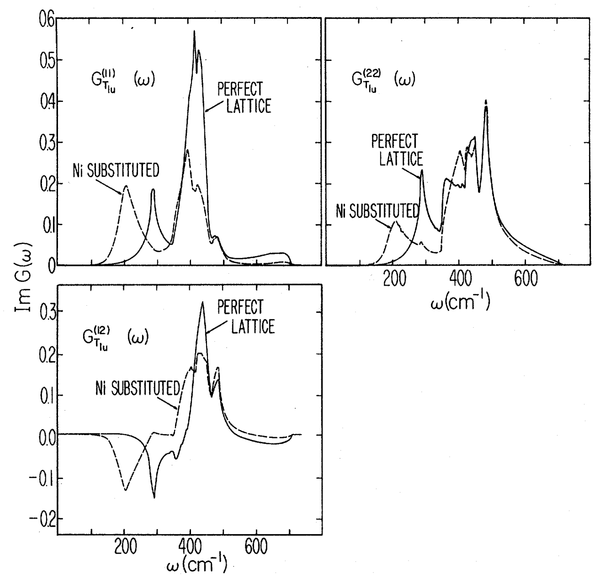

FIG. 6. The imaginary part of the T_{1u} Green's functions. In each case the solid curve gives the perfect-latice Green's function and the dashed curve is obtained when the mass of the Mg ion is replaced by that of the Ni ion without any variations in the force constants (i.e., mass change only). The vertical scale is in units of 10^{-28} sec^2 per atomic mass unit.

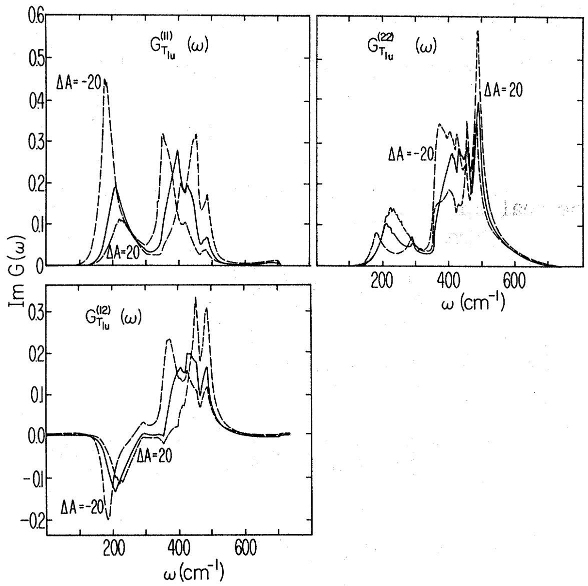

FIG. 7. The imaginary part of the T_{1u} Green's functions. The solid curve gives the defect-lattice Green's functions with mass change only (dashed curve in Fig. 6) and the dashed curves represent these functions when spring constant changes are made in addition ($\Delta B=0$).

With the new basis vectors all functions associated with $T_{1u}^{(3)}$ will have zero-coupling coefficient in the nearest-neighbor coupling scheme. Interest is, therefore, concentrated in the three Green's functions $G^{(11)}(\omega)$, $G^{(22)}(\omega)$, and $G^{(12)}(\omega)$ [$=G^{(21)}(\omega)$], and the equivalent functions in the defect lattice.

These perfect lattice functions are shown by solid curves in Fig. 6, and those corresponding to a mass change from Mg^{2+} to Ni^{2+} is given by the dashed curve. In Fig. 7, this latter trace is repeated as a solid curve and the dashed curves give examples in which additional force constant changes have been considered.

VI. COMPARISON BETWEEN THE SIDEBAND AND GREEN'S FUNCTIONS

In this section the Ni^{2+} infrared band is compared to an empirical admixture of the four odd-parity Green's functions. A comparison of Fig. 7 and Fig. 1 shows that there is a similarity between the one-phonon sideband and the $G_{T_{1u}}^{(11)}(\omega)$ function in which only mass change for the Ni^{2+} ion has been made. The likeness can be improved with slight admixtures of other Green's functions:

$$W(\omega) \propto a^2[\mathrm{Im}\,G^{(11)}_{T_{1u}}(\omega) + b^2\,\mathrm{Im}\,G^{(22)}_{T_{1u}}(\omega) + c\,\mathrm{Im}\,G^{(12)}_{T_{1u}}(\omega) + d^2\,\mathrm{Im}\,G_{T_{2u}}(\omega)], \quad (18)$$

where the coefficients are related to the square brackets in Eq. (10)

$$\left[\sum_{\gamma}\sum_{\gamma_e\gamma_f} F^{\gamma_e\to\gamma_f}_{yT^{(1)}_{1u}\gamma} F^{\gamma_e\to\gamma_f *}_{yT^{(1)}_{1u}\gamma}\right] = a^2 ,$$

$$\left[\sum_{\gamma}\sum_{\gamma_e\gamma_f} F^{\gamma_e\to\gamma_f}_{yT^{(2)}_{1u}\gamma} F^{\gamma_e\to\gamma_f *}_{yT^{(2)}_{1u}\gamma}\right] = a^2 b ,$$

$$\left[\sum_{\gamma}\sum_{\gamma_e\gamma_f} (F^{\gamma_e\to\gamma_f}_{yT^{(1)}_{1u}\gamma} F^{\gamma_e\to\gamma_f *}_{yT^{(2)}_{1u}\gamma} + F^{\gamma_e\to\gamma_f}_{yT^{(2)}_{1u}\gamma} F^{\gamma_e\to\gamma_f *}_{yT^{(1)}_{1u}\gamma})\right] = a^2 c , \quad (19)$$

$$\left[\sum_{\gamma}\sum_{\gamma_e\gamma_f} F^{\gamma_e\to\gamma_f}_{yT_{2u}\gamma} F^{\gamma_e\to\gamma_f *}_{yT_{2u}\gamma}\right] = a^2 d^2 ,$$

with $c \leqslant 2b$. For the

$$\Gamma_{3g}(^3T_{2g},\ t_g^5 e_g^3) \to \Gamma_{5g}(^3A_{2g},\ t_g^6 e_g^2)$$

transition the calculation in Sec. VII gives $c \approx 2b$, and the equality is assumed for the empirical parameters. The predominant peak positions are at 210 and 395 cm^{-1} compared to the experimental peaks at 220 and 390 cm^{-1} and have the same integrated intensities for admixture coefficients $b = 0.25$ and $d = 0$ as shown in Fig. 8. The agreement is fair but by no means exact. The largest peak matches the experimental one very well and although there are no peaks completely resolved, on its high-energy side there are clear shoulders corresponding to the calculated maxima at 430 and 480 cm^{-1}. This can be understood if there is some broadening of the features by anharmonic effects or by contributions from more distant neighbors. The peak predicted at 210 cm^{-1} agrees well for position but not so well for shape. At higher energies the peak at 550 cm^{-1} is not seen at all in the theoretical model and has not been reproduced by calculations of two phonon peaks (see Paper II). This discrepancy is probably due to an inaccuracy of the lattice-dynamical model at high frequencies. The LO branch cuts the zone boundary at 550 cm^{-1} and not at 500 cm^{-1} as given by the present model. Had parameters been used which predict this feature more accurately, then the peak at 550 cm^{-1} may well be accounted for.

By allowing for small force constant changes ΔA and ΔB or changing the admixture parameters of the Green's functions the agreement can be changed, perhaps improved, but the significance is doubtful. It is interesting in this context that Sangster and McCombie[8] have obtained an alternative fit by allowing for force constant changes rather than admixture of Green's functions. Clearly, it would be desirable to determine independently one or both sets of parameters (i.e., force constant changes and/or Green's-function coupling parameters). In Sec. VII the results of a calculation of the latter are described.

VII. COUPLING PARAMETERS

A theoretical determination of the admixtures of Green's functions requires an evaluation of the parameters $F^{\gamma_e\to\gamma_f}_{y\Gamma\gamma n}$ and for this to be consistent with our justification for assuming that the perturbation arises predominantly from the motion of the Ni^{2+} ion and its six nearest neighbors, a molecular orbital treatment should be adopted. This has not been attempted, but rather it is assumed that the interaction is proportional to the change in electrostatic potential at the participating electron arising from the relative motion of the central ion and nearest neighbor ions considered as point charges.

In addition, to simplify the calculation, it was assumed that the higher-energy odd-parity states of the Ni^{2+} ion lie sufficiently far above the d^8 configuration levels and sufficiently close together that the energy denominator in (8) may be taken to be the same for all terms, i.e.,

$$\mathcal{E}_i - \mathcal{E}_e \simeq \mathcal{E}_i - \mathcal{E}_f \simeq \Delta\mathcal{E} \quad \text{for all } i . \quad (20)$$

For Ni^{2+} in MgO the upper states lie within a region of strong absorption by the lattice starting at 40 000 cm^{-1}, and are not directly accessible to measurement. However, in the free ion the lowest

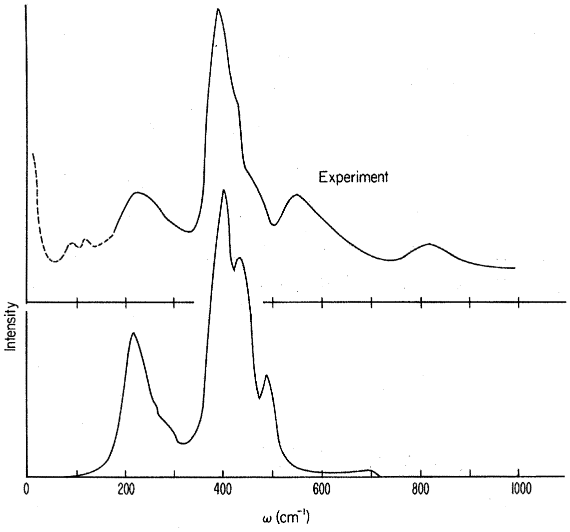

FIG. 8. Comparison between experimental sideband and calculated sideband. The following empirical admixture of the T_{1u} Green's functions is used: $1G^{(1,1)}_{T_{1u}}(\omega) + 0.25G^{(12)}_{T_{1u}}(\omega) + 0.025G^{(2,2)}_{T_{1u}}(\omega)$. The peak at 550 cm^{-1} is thought to be a one-phonon feature but the 800-cm^{-1} peak is more likely to arise from a two-phonon process.

odd-parity state (d^7p) is at 110 000 cm^{-1} and the ionization limit lies at 310 000 cm^{-1}.[24] Assuming the crystal field levels do not drastically alter these then the conditions will be partially realized.

The summation in Eq. (8) is over all excited states i (only odd electronic states contributing), and therefore, because the energy denominator is the same for each term, closure may be used:

$$\sum_{a_i\Gamma_i\gamma_i} |a_i\Gamma_i\gamma_i\rangle\langle a_i\Gamma_i\gamma_i| = 1 \; . \tag{21}$$

The electric dipole operator commutes with the electrostatic perturbation $V_{\Gamma\gamma}^{(n)}$, and hence:

$$F_{y\Gamma\gamma n}^{\gamma_e\to\gamma_f} = (2/\Delta\mathcal{E})\langle\Gamma_f\gamma_f|yV_{\Gamma\gamma}^{(n)}|\Gamma_e\gamma_e\rangle \; . \tag{22}$$

By making use of symmetry, the number of matrix elements which need be evaluated can be greatly reduced. For example, considering the transition from a doubly degenerate Γ_{3g} level to a triply degenerate Γ_{5g} level, the coupling can be determined by evaluating the following elements:

$$F_{y\Gamma\gamma n}^{\zeta\to\epsilon} = (2/\Delta\mathcal{E})\langle\Gamma_{5g}\zeta|yV_{\Gamma\gamma}^{(n)}|\Gamma_{3g}\epsilon\rangle, \qquad \Gamma\gamma = T_{1u}x\,, \;\; T_{2u}\xi \tag{23}$$

$$F_{y\Gamma\gamma n}^{\zeta\to\theta} = (2/\Delta\mathcal{E})\langle\Gamma_{5g}\zeta|yV_{\Gamma\gamma}^{(n)}|\Gamma_{3g}\theta\rangle, \qquad \Gamma\gamma = T_{1u}x, \;\; T_{2u}\xi \tag{24}$$

where the two Γ_{3g} or E_g functions are denoted by θ, ϵ angular parts transforming as $(3z^2 - r^2)$ and $(x^2 - y^2)$, respectively, and the three Γ_{5g} or Γ_{2g} functions are denoted by the ξ, η, and ζ angular parts transforming as yz, zx, and xy, respectively.

The total coupling coefficient [bracketed term in Eq. (10)] for the Green's function $G_\Gamma^{(nn')}(\omega)$ is then given by

$$2[F_{y\Gamma\gamma n}^{\zeta\to\epsilon}F_{y\Gamma\gamma n'}^{\zeta\to\epsilon *} + F_{y\Gamma\gamma n}^{\zeta\to\theta}F_{y\Gamma\gamma n'}^{\zeta\to\theta *}] \; . \tag{25}$$

To proceed further some form of the electrostatic potential and suitable electronic wave functions must be adopted. Details of these follow.

A. Vibrational Perturbation

Introducing the basis set in Fig. 5, the change in potential energy at the $3d$ electron is given for each vibration by[25]

$$V_{T_{1u}x}^{(A)} = -\frac{1}{2}\left[4\mathcal{Y}_1^1\frac{\vec{r}}{R^3} + (-2\sqrt{6}\,\mathcal{Y}_3^1 + 2\sqrt{10}\,\mathcal{Y}_3^3)\frac{\vec{r}^3}{R^5} + \left(\frac{3\sqrt{15}}{2}\,\mathcal{Y}_5^1 - \frac{3\sqrt{35}}{2\sqrt{2}}\,\mathcal{Y}_5^3 + \frac{3\sqrt{63}}{2\sqrt{2}}\,\mathcal{Y}_5^5\right)\frac{\vec{r}^5}{R^7}\right]Ze^2 \,, \tag{26}$$

$$V_{T_{1u}x}^{(B)} = \frac{1}{2}\left[4\mathcal{Y}_1^1\frac{\vec{r}}{R^3} + \left(\frac{3\sqrt{6}}{2}\,\mathcal{Y}_3^1 - \frac{3\sqrt{10}}{2}\,\mathcal{Y}_3^3\right)\frac{\vec{r}^3}{R^5} + \left(\frac{9\sqrt{15}}{4}\,\mathcal{Y}_5^1 + \frac{3\sqrt{35}}{4\sqrt{2}}\,\mathcal{Y}_5^3 + \frac{15\sqrt{7}}{4\sqrt{2}}\,\mathcal{Y}_5^5\right)\frac{\vec{r}^5}{R^7}\right]Ze^2, \tag{27}$$

$$V_{T_{2u}\xi} = -\frac{1}{2}\left[\left(\frac{5\sqrt{6}}{2}\,\mathcal{Y}_3^1 + \frac{3\sqrt{10}}{2}\,\mathcal{Y}_3^3\right)\frac{\vec{r}^3}{R^5} + \left(\frac{7\sqrt{15}}{4}\,\mathcal{Y}_5^1 + \frac{3\sqrt{35}}{4\sqrt{2}}\,\mathcal{Y}_5^3 + \frac{15\sqrt{7}}{4\sqrt{2}}\,\mathcal{Y}_5^5\right)\frac{\vec{r}^5}{R^7}\right]Ze^2 \,, \tag{28}$$

where Ze is the electrostatic charge on each of the nearest neighbors, each at distance R. The electron coordinate is $\vec{r}$ referred to the core position as origin: $\mathcal{Y}_l^m$ is defined as

$$\mathcal{Y}_l^m = \left(\frac{4}{2l+1}\right)^{1/2}\left[\frac{Y_l^{-m} - Y_l^m}{2}\right], \tag{29}$$

where Y_l^m are spherical harmonics.

In the choice of T_{1u} basis vectors used in the Green's-function calculation (Fig. 5), the corresponding perturbations are related to the above ones by

$$V_{T_{1u}x}^{(1)} = (2\sqrt{2}/\sqrt{3})\,V_{T_{1u}x}^{(B)} + \sqrt{3}\,V_{T_{1u}x}^{(A)} \,, \tag{30}$$

$$V_{T_{1u}x}^{(2)} = (\sqrt{7}/\sqrt{3})\,V_{T_{1u}x}^{(B)} \; . \tag{31}$$

B. Electronic Wave Functions

The electronic wave functions $|\Gamma_e\gamma_e\rangle$, $|\Gamma_f\gamma_f\rangle$ are given in the standard form by crystal field theory as the eigenstates of the Liehr and Ballhausen energy matrices [Ref. 26, Eq. (4)]. With the parameters $F_4 = 100$ cm^{-1}, $F_2 = 1400$ cm^{-1}, $Dq = -830$ cm^{-1}, and $\lambda = -325$ cm^{-1} which were parameters chosen to predict the Γ_{3g} and Γ_{4g} levels at 8002 and 8178 cm^{-1},[20] the relevant eigenstates expressed as a linear combination of strong field states are

$$|\Gamma_5\rangle = 0.988|\Gamma_5(^3A_2\,t_2^6e^2)\rangle + 0.106|\Gamma_5(^3T_2\,t_2^5e^3)\rangle + 0.002|\Gamma_5(^3T_1t_2^5e^3)\rangle + 0.028|\Gamma_5(^1T_2\,t_2^5e^3)\rangle + 0.005|\Gamma_5(^3T_2t_2^4e^4)\rangle + 0.000|\Gamma_5(^1T_2\,t_2^4e^4)\rangle \,, \tag{32}$$

$$|\Gamma_3\rangle = 0.965|\Gamma_3(^3T_2t_2^5e^3)\rangle + 0.115|\Gamma_3(^1Et_2^6e^2)\rangle + 0.088|\Gamma_3(^3T_1t_2^5e^3)\rangle + 0.118|\Gamma_3(^3T_1t_2^4e^4)\rangle + 0.010|\Gamma_3(^1Et_2^4e^4)\rangle \,, \tag{33}$$

where, because the eigenstates are the same for each row of the irreducible representation, the label for the row has not been included. Also, for brevity the suffix g is dropped.

The strong field states can be expressed in terms of the product wave functions of two-hole wave functions, e.g.,

$$|\Gamma_5\zeta(^3A_2t_2^6e^2)\rangle = -(i/\sqrt{2})(|\theta^+\epsilon^-\rangle + |\theta^-\epsilon^+\rangle) \,, \tag{34}$$

$$|\Gamma_3\theta({}^3T_2t_2^5e^3)\rangle=\tfrac{1}{4}i(|\theta^+\xi^+\rangle-\sqrt{3}\,|\epsilon^+\xi^+\rangle+i|\theta^+\eta^+\rangle+i\sqrt{3}\,|\epsilon^+\eta^+\rangle-|\theta^-\xi^-\rangle+\sqrt{3}\,|\epsilon^-\xi^-\rangle+i|\theta^-\eta^-\rangle+i\sqrt{3}\,|\epsilon^-\eta^-\rangle)\,, \quad (35)$$

$$|\Gamma_3\epsilon({}^3T_2t_2^5e^3)\rangle=(i/2\sqrt{12})$$
$$\times\,[\tfrac{1}{2}|\theta^+\xi^+\rangle-(\sqrt{3}/2)|\epsilon^+\xi^+\rangle-\tfrac{1}{2}i\,|\theta^+\eta^+\rangle-\tfrac{1}{2}i\sqrt{3}\,|\epsilon^+\eta^+\rangle$$
$$-\tfrac{1}{2}|\theta^-\xi^-\rangle+(\sqrt{3}/2)|\epsilon^-\xi^-\rangle-\tfrac{1}{2}i|\theta^-\eta^-\rangle-(i\sqrt{3}/2)|\epsilon^-\eta^-\rangle-4|\theta^+\zeta^-\rangle-4|\theta^-\zeta^+\rangle]\,, \quad (36)$$

where + and − denote spin projection.

C. Coupling Parameters

Upon evaluation of the angular dependence, the matrix elements (23) and (24) can be expressed in terms of a product of the constant $Ze^2/R\Delta\mathcal{E}$ and the weighted sum of three radial integrals:

$$R_2=\langle r^2\rangle/R^2;\quad R_4=\langle r^4\rangle/R^4;\quad R_6=\langle r^6\rangle/R^6\,. \quad (37)$$

Unfortunately, there is significant variation in the values of these integrals depending from what type of calculation they are taken,[25] e.g., using analytical Slater functions or Hartree-Fock functions. However, no attempt is made to calculate absolute intensities and the relative coupling coefficients depend only on the relative $R_2/R_4/R_6$ values. In addition, it will be shown below that for the

$$\Gamma_{3g}({}^3T_{2g}\,,\ t_g^5e_g^3)\to\Gamma_{5g}({}^3A_{2g}\,,\ t_g^6e_g^2)$$

transition the coupling parameters are insensitive to the value of R_2.

The largest contribution to matrix elements (23) and (24) should arise from the first of the strong-field states in the eigenstates (32) and (33). Consider the contribution from these terms only, i.e., in the strong-field limit,

$$F^{\xi\to\epsilon}_{y\Gamma\gamma n}=(2/\Delta\mathcal{E})\langle\Gamma_5\zeta({}^3A_2\,t_2^6e^2)|\,yV^{(n)}_{\Gamma\gamma}|\,\Gamma_3\epsilon({}^3T_2t_2^5e^3)\rangle, \quad (38)$$

where

$$\Gamma\gamma=T_{1u}x,\ T_{2u}\xi\ ,$$

$$F^{\xi}_{y\Gamma\gamma n}=(2/\Delta\mathcal{E})\,\langle\Gamma_5\zeta({}^3A_2\,t_2^6e^2)|\,yV^{(n)}_{\Gamma\gamma}|\,\Gamma_3\theta({}^3T_2\,t_2^5e^3)\rangle\ , \quad (39)$$

where

$$\Gamma\gamma=T_{1u}x,\ T_{2u}\xi\ .$$

It can be seen by inspecting the spin components [see Eqs. (34)–(36)] that the $F^{\xi\to\theta}$'s are all zero and the $F^{\xi\to\epsilon}$'s have only a contribution from the last line of (36):

$$F^{\xi\to\epsilon}_{y\Gamma\gamma n}=\frac{2}{\Delta\mathcal{E}}\,\frac{1}{\sqrt{6}}\ \ (\langle\epsilon^+|\,yV^{(n)}_{\Gamma\gamma}|\,\zeta^+\rangle+\langle\epsilon^-|\,yV^{(n)}_{\Gamma\gamma}|\,\zeta^-\rangle) \quad (40)$$

$$=\frac{2}{\Delta\mathcal{E}}\,\frac{2}{\sqrt{6}}\ \langle\epsilon|\,yV^{(n)}_{\Gamma\gamma}|\,\zeta\rangle\ . \quad (41)$$

The spin dependence of the one-electron wave functions can be dropped because the operators have only orbital dependence. Note that is because $F^{\xi\to\theta}$ is zero that the parameter for the cross Green's function $G^{(12)}_{T1u}(\omega)$ is equal to $2b$. When using the eigenstates, both elements, i.e., (23) and (24), are nonzero and the cross-term parameter is no longer exactly $2b$. However, (23) remains small compared to (24), and the resultant deviation from $2b$ is slight, as will be seen from Table II.

Evaluation of the one-electron matrix elements in (41) gives

$$F^{\xi\to\epsilon}_{y\,T^{(1)}_{1u}x}=\frac{4}{\sqrt{6}}\left[-\frac{15}{7}\,\frac{\sqrt{2}}{\sqrt{3}}\,R_4+\frac{10}{11}\,\frac{\sqrt{2}}{\sqrt{3}}\,R_6\right]\frac{Ze^2}{R\Delta\mathcal{E}}\ , \quad (42)$$

$$F^{\xi\to\epsilon}_{y\,T^{(2)}_{1u}x}=\frac{4}{\sqrt{6}}\left[-\frac{5}{14}\,\frac{\sqrt{7}}{\sqrt{3}}\,R_4-\frac{10}{22}\,\frac{\sqrt{7}}{\sqrt{3}}\,R_6\right]\frac{Ze^2}{R\Delta\mathcal{E}}\ , \quad (43)$$

$$F^{\xi\to\epsilon}_{y\,T_{2u}}=\frac{4}{\sqrt{6}}\left[\frac{1}{2}\,\frac{5}{7}\,R_4+\frac{1}{2}\,\frac{10}{11}\,R_6\right]\frac{Ze^2}{R\Delta\mathcal{E}}\ . \quad (44)$$

Note that the coefficients of the R_2 terms always vanish. This result may be obtained from symmetry arguments in the full rotation group and is not, therefore, a property restricted to the nearest-neighbor treatment. It implies that the dipole

TABLE II. Coupling parameters. The numbers outside the brackets give the coupling coefficients using the eigenstates given in Eqs. (32) and (33), and the numbers in the brackets are the corresponding coefficients using strong-field wave functions as in the calculation in the text.

	Ratio of radial integrals	Coupling parameters relative to the $G^{(11)}_{T_{1u}}(\omega)$ parameter			
	$R_6:R_4:R_2$	$G^{(11)}_{T_{1u}}(\omega)$	$G^{(12)}_{T_{1u}}(\omega)$	$G^{(22)}_{T_{1u}}(\omega)$	$G_{T_{2u}}(\omega)$
Notation		a^2	a^2c	a^2b^2	a^2d^2
Set I	1 : 5 : 25	1	0.91 (0.85)	0.21 (0.20)	0.08 (0.08)
Set II	0 : 5 : 25	1	0.66 (0.62)	0.12 (0.10)	0.04 (0.04)
Empirical parameters		1	0.25	0.025	0.0

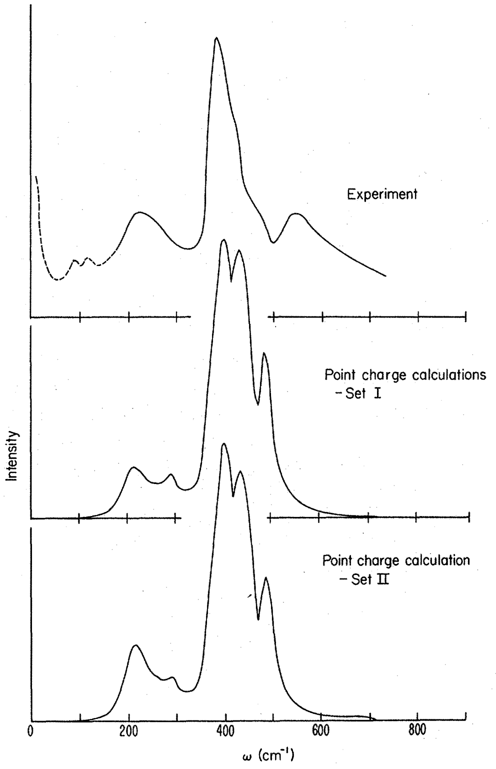

FIG. 9. Comparison between experimental sideband and admixture of odd Green's functions as predicted by a point-charge calculation (see text). Sets I and II correspond to values in Table II.

terms in the strong-field limit do not contribute. Rather the octopole terms are dominant. These drop off with distance $1/R^5$ and hence little contribution would be expected from neighbors more distant than the nearest ones.

The coupling parameters' dependence on the R_6/R_4 ratio can be seen from Eqs. (42)–(44). For $R_6/R_4 = 0$, the $T_{1u}^{(1)}$ coupling coefficient is a factor 3.2 larger than the $T_{1u}^{(2)}$ coupling factor, and a factor 5 larger than the one for T_{2u}. As the R_6/R_4 ratio is increased to 0.7 the two T_{1u} coefficients become equal but still more than twice as large than for the T_{2u}.

This calculation is repeated using the eigenstates (32) and (33) rather than the strong-field approximation. The results are given in Table II for certain choices of $R_2/R_4/R_6$ ratios. Set I gives the parameters for a probable ratio and Set II is included to show their dependence on the R_4/R_6 ratio. The values are very close to the ones given in brackets obtained in the strong-field case, and the conclusion that octopole terms predominate is still valid.

Sidebands are constructed using these sets of parameters and the results are shown in Fig. 9. This is done for both sets to show that a variation of the parameters within such limits does not drastically alter the band shape. Considering the crudeness of the coupling model, the agreement is considered to be very satisfactory, especially when small changes in force constants ΔA and ΔB could presumably be introduced to further improve the fit.

VIII. CONCLUSIONS

In this paper a reasonably successful attempt has been made at correlating an observed one-phonon vibronic band with a theoretical calculation based on the lattice dynamics of MgO.

These results were obtained by using a nearest-neighbor-coupling interaction. It would be wrong, however, to conclude from this alone that a short-range interaction necessarily applies for all $3d^n \to 3d^n$ vibronic transitions. This is because the interaction, in the case of the $\Gamma_{3g}(^3T_{2g}) \to \Gamma_{5g}(^3A_{2g})$ transition of Ni^{2+}, may be more strongly localized than is usual for $3d^n \to 3d^n$ transitions. Here octopole terms predominate. In general, it is more likely that the dipole terms will give the largest contribution. On the other hand, this is not to say that a nearest-neighbor interaction should not still be sufficient to describe other transitions accurately.

The nagging weakness in the theoretical computation of the sideband is the employment of too numerous parameters. An attempt at evaluating some of these, namely the coupling parameters, from a simple point-charge model has been shown to correlate remarkably well with those determined empirically. Similar success is claimed by Sangster and McCombie[8] for a V^{2+} transition. However, this is not repeated in a second Ni^{2+} transition.[17] Whether there is another explanation for the lack of agreement in this latter case or the results in the former two cases are fortuitous is unclear. It is certainly difficult to wholly justify the model adopted although it is analogous to the use of the point-charge model in static crystal field theory.

ACKNOWLEDGMENTS

I would like to acknowledge the advice and encouragement of Dr. R. W. H. Stevenson, Professor C. McCombie, and Dr. M. J. Sangster for the use of their computer calculation of Green's functions. Thanks also to my colleagues at Aberdeen and U. C. L. A. for many useful discussions.

---

†Research conducted at University of Aberdeen supported by the Science Research Council and at UCLA supported by U. S. Army Research Office, Durham, N. C.

*Now at Queen Mary College, London, England.

[1] T. Timusk and M. Buchanan, Phys. Rev. 164, 345 (1967).

[2] W. E. Bron, Phys. Rev. 185, 1163 (1969).

[3] W. E. Bron and Max Wagner, Phys. Rev. 167, 841 (1968).

[4] Max Wagner, Z. Physik 214, 78 (1968).

[5] M. Buchanan and E. J. Woll, Jr., Can. J. Phys. 47, 1757 (1969).

[6] J. B. Page, Jr. and B. G. Dick, Phys. Rev. 163, 910 (1967).

[7] J. B. Page, Jr. and D. Strauch, Phys. Status Solidi 24, 469 (1967).

[8] M. J. L. Sangster and C. W. McCombie, J. Phys. C 3, 1498 (1970).

[9] J. E. Ralph and M. G. Townsend, J. Chem. Phys. 48, 149 (1968).

[10] J. E. Ralph and M. G. Townsend, J. Phys. C 3, 8 (1970).

[11] M. D. Sturge, Phys. Rev. 130, 639 (1963).

[12] G. F. Imbusch, M. L. Report No. 1190, Stanford University, 1964 (unpublished).

[13] A. M. Glass and T. M. Searle, J. Chem. Phys. 46, 2092 (1967).

[14] G. Peckham, Proc. Phys. Soc. (London) 90, 657 (1967).

[15] R. J. Buckland and D. H. Saunderson, Atomic Energy Research Establishment, Harwell, Report No. R-5467, 1967 (unpublished).

[16] R. E. Watson and A. J. Freeman, Phys. Rev. 134, A1526 (1964); S. Sugano and R. G. Shulman, *ibid.* 130, 517 (1963).

[17] N. B. Manson, following Paper, Phys. Rev. B 4, 2656 (1971).

[18] R. Pappalardo, D. L. Wood, and R. C. Linares, J. Chem. Phys. 35, 1460 (1961).

[19] W. Low, Phys. Rev. 109, 247 (1958).

[20] N. B. Manson, Ph. D. thesis (University of Aberdeen, 1968) (unpublished).

[21] H. A. Jahn and E. Teller, Proc. Roy. Soc. (London) A161, 220 (1937).

[22] J. E. Wertz, J. W. Orton, and P. Auzins, J. Appl. Phys. Suppl. 33, 322 (1962).

[23] The shell and core displacements between 0 and 500 cm^{-1} are not significantly different and hence the core-core, core-shell, and shell-shell Green's functions are similar. Above 500 cm^{-1} the negative-ion's shell displacements are typically half that of its core, but there is only little intensity in this region without any pronounced features and, therefore, it does not destroy the over-all similarity between the core and shell Green's functions.

[24] A. G. Shenstone, J. Opt. Soc. Am. 44, 749 (1954).

[25] S. Koide and M. H. L. Pryce, Phil. Mag. 3, 607 (1958).

[26] A. D. Liehr and C. J. Ballhausen, Ann. Phys. (N. Y.) 6, 134 (1959).

PHYSICAL REVIEW B VOLUME 4, NUMBER 8 15 OCTOBER 1971

Multiphonon Vibronic Transition ${}^1T_{2g}$-${}^3A_{2g}$ of Ni^{2+} in MgO†

N. B. Manson*
Department of Physics, University of California, Los Angeles, California 90024

(Received 1 June 1970)

The $\Gamma_{5g}({}^1T_{2g}, t_{2g}^5 e_g^3)$-$\Gamma_{5g}({}^3A_{2g}, t_{2g}^6 e_g^2)$ vibronic spectrum is recorded in absorption and emission—under x-ray excitation—at crystal temperatures of 77 and 5 °K. The spectrum involves up to four phonon processes and a theoretical treatment of such a transition is presented. A possible explanation of the band is suggested and, by using imperfect-lattice Green's functions for the nearest-neighbor motion, it is constructed to give excellent agreement with experiment. The transition is forced (electric dipole) by one of the T_{1u} vibrations of the nearest-neighbor complex. Additional E_g vibrations couple in the higher phonon processes which suggest the presence of a Jahn-Teller distortion in the ${}^1T_{2g}$ excited state. However, it has not been possible to establish the presence of such a Jahn-Teller distortion from any other experimental data. A similar calculation is undertaken for the two-phonon band of the $\Gamma_{3g}({}^3T_{2g}, t_{2g}^5, e_g^3)$-$\Gamma_{5g}({}^3A_{2g}, t_{2g}^6 e_g^2)$ transition of Ni^{2+} in MgO. Again there is an indication of a coupling to E_g vibrations in the two-phonon process.

I. INTRODUCTION

In Paper I[1] the vibronic band associated with the single electronic transition $\Gamma_{3g}({}^3T_{2g}, t_{2g}^5 e_g^3)$-$\Gamma_{5g}({}^3A_{2g}, t_{2g}^6 e_g^2)$ of MgO:Ni^{2+} is studied and good agreement is obtained between the one-phonon structure and that predicted by a Green's-function treatment of the motion of the impurity ion and its six nearest neighbors. In this paper the calculations are extended to consider higher-order phonon processes; the main focus of attention being $\Gamma_{5g}({}^1T_{2g}, t_{2g}^5 e_g^3)$-$\Gamma_{5g}({}^3A_{2g}, t_{2g}^6 e_g^2)$ vibronic transitions in MgO:Ni^{2+}. In this case both states are well isolated from other electronic levels and the vibronic band associated with this single electronic transition is seen very clearly in emission, weakly in absorption. A possible construction of the band is proposed. It is constructed with localized Green's functions using semiempirical parameters and compared to the observed band. A similar treatment for the two-phonon sideband of the $\Gamma_{3g} \rightarrow \Gamma_{5g}$ is presented and a comparison made between the